

REPORT DOCUMENTATION PAGE			Form Approved OMB No. 0704-0188	
Public reporting burden for the collection of information is estimated to average 1 hour per response, including the time for reviewing instructions, searching existing data sources, gathering and maintaining the data needed, and completing and reviewing the collection of information. Send comments regarding this burden estimate or any other aspect of this collection of information, including suggestions for reducing this burden, to Washington Headquarters Services, Directorate for Information Operations and Reports, 1215 Jefferson Davis Highway, Suite 1204, Arlington, VA 22202-4302, and to the Office of Management and Budget, Paperwork Reduction Project (0704-0188), Washington, DC 20503.				
1. AGENCY USE ONLY (Leave blank)		2. REPORT DATE June 1993		3. REPORT TYPE AND DATES COVERED
4. TITLE AND SUBTITLE Anechoic Chamber Simulation and Verification			5. FUNDING NUMBERS	
6. AUTHOR(S) Taylor, Robert. M.				
7. PERFORMING ORGANIZATION NAME(S) AND ADDRESS(ES) Computer Sciences Corporation 190 S Wolfe Ave, Bldg 1260 Edwards AFB CA 93524			8. PERFORMING ORGANIZATION REPORT NUMBER	
9. SPONSORING / MONITORING AGENCY NAME(S) AND ADDRESS(ES) California State University at Northridge			10. SPONSORING / MONITORING AGENCY REPORT NUMBER	
11. SUPPLEMENTARY NOTES				
12a. DISTRIBUTION / AVAILABILITY STATEMENT Distribution authorized for public release			12b. DISTRIBUTION CODE A	
13. ABSTRACT (Maximum 200 words) <p>This project considers an electromagnetic field simulation of an anechoic chamber with verification measurements. The simulation is a Geometric Optics (Ray Tracing) mathematical model of the direct path between two antennae and interfering scattering. There are two separate models due to the frequency dependent nature of the pyramidal absorbing material. The measurements and simulations were based on an azimuth cylindrical scan. The model for the frequency range of 30 to 500 MHz was used to characterized lossy specular scattering as a lossy, tapered, TEM transmission line in an inhomogeneous, anisotropic, tensor material. The frequency range of 500 MHz to 18 GHz was characterized by dominant tip diffraction of RAM patches, and the model made use of a Uniform Theory of Diffraction code for a dielectric corner.</p> <p>19960513 072</p>				
14. SUBJECT TERMS Anechoic Chamber Radar Absorbing Material (RAM) Uniform Theory of Diffraction			15. NUMBER OF PAGES 61	
			16. PRICE CODE	
17. SECURITY CLASSIFICATION OF REPORT UNCLASSIFIED	18. SECURITY CLASSIFICATION OF THIS PAGE UNCLASSIFIED	19. SECURITY CLASSIFICATION OF ABSTRACT UNCLASSIFIED	20. LIMITATION OF ABSTRACT SAR	

CALIFORNIA STATE UNIVERSITY, NORTHRIDGE

ANECHOIC CHAMBER SIMULATION AND VERIFICATION

A project submitted in partial fulfillment of the requirements for the degree of
Master of Science in Engineering

by

Robert M. Taylor

June, 1993

CALIFORNIA STATE UNIVERSITY, NORTHRIDGE

ANECHOIC CHAMBER SIMULATION AND VERIFICATION

A project submitted in partial fulfillment of the requirements for the degree of
Master of Science in Engineering

by

Robert M. Taylor

June, 1993

The Project of Robert M. Taylor is approved:

<u>Tarek Shraibati</u>	<u>5-11-93</u>
Tarek Shraibati	Date

<u>Sembiam R. Rengarajan</u>	<u>5-11-93</u>
Sembiam R. Rengarajan	Date

<u>Edmond S. Gillespie</u>	<u>5-11-93</u>
Edmond S. Gillespie (Chair)	Date

California State University, Northridge

ACKNOWLEDGMENTS

The author would like to express his appreciation to Computer Sciences Corporation, Advanced Technology Division and the Air Force Flight Test Center, Edwards Air Force Base, California for the support of the project development and facilities use at the Benefield Anechoic Chamber. Special thanks are given to Chris Holloway for his help in providing references for the low frequency modeling. Special thanks are given to Dr. Sembiam Rengarajan and Dr. Edmond S. Gillespie for their guidance. Special thanks are given to Philip Joseph and the Air Force Institute of Technology for help in providing references and the TIPBIST subroutine software used in the high frequency modeling.

TABLE OF CONTENTS

	PAGE
ACKNOWLEDGEMENT	iii
ABSTRACT	v
LIST OF FIGURES	vi
INTRODUCTION	1
1. CHAMBER MODEL GEOMETRY	4
A. Low Frequency and High Frequency Model Geometry Contrast	7
B. RAM Models	10
C. Geometry of the Walls	11
2. LOW FREQUENCY SIMULATION	18
A. RAM Model	19
B. Computer Resources	22
C. Polarization and Orientation Considerations	23
D. Source and Receive Antennas	26
E. Number of Data Points	27
3. HIGH FREQUENCY SIMULATION	28
A. RAM Model	29
B. Back Wall	31
C. Computer Resources	31
D. Receive and Source Antenna	34
E. Number of Data Points	37
4. MODAL EXPANSION	37
5. MEASUREMENT CONFIGURATION	38
6. DATA COMPARISONS	42
A. Data Correlation	43

B. Resolving Discrepancies	47
7. CONCLUSIONS	47
A. Recommendations	47
B. Summary	48
REFERENCES	50

TABLE OF FIGURES

FIGURES	PAGE
1. Anechoic Chamber Configuration	
Showing Multipath Effects in the Quiet Zone	5
2. Wall Geometry	5
3. Cylindrical Scan	6
4. Cylindrical Scan Geometry	6
5. Specular Reflection Through Pyramidal RAM	9
6. Method of Images	9
7. Dominant Tip Diffraction for High Frequency Model	9
8. RAM Patch Top View Showing Local Coordinate System of Tip 5	9
9. High Frequency RAM Tip Coordinate System	12
10. RAM Dimensions for Low Frequency Model	12
11. Taper Geometry for Low Frequency Model	12
12. Twisted RAM Geometry	12
13. Floor Geometry	15
14. East Wall Geometry	15
15. West Wall Geometry	16
16. Ceiling Geometry	16
17. Back Wall Geometry	17
18. Transverse, Periodic, Rectangular, Lossy Rods Used in Low Frequency Formulation	24
19. Flow Chart for Low Frequency Model	24
20. Floor Polarization Orientation	25
21. East Wall Polarization Orientation	25
22. Side View of Wedge	32

23. Oblique Incidence of Wedge	32
24. Corner Diffraction on a Wedge	32
25. Polarization used on Wedge Corner Diffraction, Upper Plot Is Incident Orientation and the Lower Plot is Scattered Orientation.	32
26. Flow Chart for High Frequency Model	33
27. Diagonal Horn Modes	35
28. Diagonal Horn Antenna Coordinate System	35
29. Measurement Equipment Block Diagram	39
30. Location of the S/A Positioner in the Chamber	40
31. Positioner Configuration with Antenna Fixture	40
32. Low Frequency Dipole Antenna Tuning	41
33. High Frequency Sleeve Dipole Antenna Tuning	41
34. Low Frequency Comparison of Simulated and Measured Data	44
35. Low Frequency Simulation without Chamber Antennas	44
36. High Frequency Comparison of Simulated and Measured Data	45
37. High Frequency Simulation	45
38. High Frequency Measurement	46
39. Modal Expansion Showing Phase Convergence in -90° to -180°	46

ABSTRACT

ANECHOIC CHAMBER SIMULATION AND VERIFICATION

by

ROBERT M. TAYLOR

Master of Science in Electrical Engineering

This project considers an electromagnetic field simulation of an anechoic chamber, electromagnetic field simulation with verification measurements. The simulation is a Geometric Optics (Ray Tracing) mathematical model of the direct path between two antennas and interfering scattering. There are two separate models due to the frequency dependent nature of the pyramidal radar absorbing material (RAM). The model for the frequency range of 30 to 500 MHz was used to characterize the lossy specular scattering. The specular scattering was modeled as a lossy, tapered, TEM transmission line in an inhomogeneous anisotropic tensor material. The frequency range from 500 MHz to 18 GHz was characterized by dominant tip diffraction of RAM patches and the model made use of a Uniform Theory of Diffraction code for a dielectric, corner. The measurements and simulations were based on an azimuthal cylindrical scan. Diagnostic measurements were also performed by a cylindrical scan of a directional horn antenna to locate scattering sources in the chamber. A cylindrical wave, modal expansion of the diagnostic data which included a one dimensional Fast Fourier Transform with Hankel function expansions.

ANECHOIC CHAMBER SIMULATION AND VERIFICATION

INTRODUCTION

The performance of an anechoic chamber can be limited by the imperfections in the radar absorbing materials (RAM) or other chamber scattering sources. Measurements to characterize the imperfections are conventionally in quantities of amplitude or phase ripple, amplitude taper or site attenuation deviation (SAD) within a test zone or quiet zone. Diagnostic measurements such as free-space standing wave ratio (SWR) measurements, site attenuation comparisons, time-domain reflectometry, pattern comparisons, plane wave spectral (PWS), and inverse synthetic aperture radar (ISAR) imaging, can be used to locate interfering sources and corrections can be made.

It is useful to predict the electromagnetic field characteristics of the chamber with mathematical models to aid in the design of the chamber or the strategic placement of RAM. The Geometric Optics (GO) or ray tracing technique has been applied to tapered chambers [1], rectangular chambers [2]-[8], low frequency, site attenuation chambers [9], and to indoor compact ranges [10]. A modification to the conventional ray tracing, infinitely thin, ray model to a reflection cone model has been suggested [11] to include curved surfaces in a chamber. Ray tracing has been combined with Uniform Theory of Diffraction (UTD) for a dielectric corner in a compact range [12], [13]. A finite element formulation has been suggested for anechoic chamber analysis [14] though the initial study was in waveguide. The method of moments has been applied to the analysis of four-wire anechoic chambers [15] and [16]. The finite-difference time domain technique has been used to study four-wire anechoic chambers [16] and rectangular chambers [3] and [17], and a finite-difference frequency domain technique has been useful in analyzing low frequency shielded semi-

anechoic chambers [18]. A Transverse Electromagnetic (TEM) wave model has also been found useful in analyzing four-wire chambers [19]. Time domain predictions have been used to improve a compact range performance [20]. Finite-range gain equations have been used to evaluate chamber range antenna effectiveness [21]. A model management system has been developed [22] for Electronic Warfare (EW) simulation type chambers to include not only the multipath interference of the chamber walls, but also includes effects as System Under Test (SUT) interaction with the chamber, and pulse transmission characteristics.

A key component of the chamber simulation was the RAM model for which various methods have been used to predict the RAM characteristics. Some models specifically generated for pyramidal RAM are tapered transmission line models with increasing attenuation toward a conducting wall [23]-[25], UTD for corner diffraction [12] and [13], propagation in uniform and lossy dielectric layers, Boundary Element Method (BEM), radiating structures, periodic method of moments (PMM), finite element, and statistical methods, of which the first two techniques were used extensively for this project. The following paragraph gives a brief overview of the highlights of the project.

This project was a study of an anechoic chamber, computer simulation for predicting the electromagnetic field characteristics within a test or quiet zone (figure 1). Samples of the field were collected by a cylindrical scan and plotted in amplitude. The effects of amplitude taper, amplitude ripple and phase were included. Ray tracing was used to simulate a propagating wave from a stationary range antenna to a receive probe antenna over a direct path, the specular paths from the walls, floor or ceiling forward of the range antenna, and paths to pyramidal RAM tips. The simulation was divided into low and high frequency models because of the frequency dependant nature of the RAM characteristics. The low frequency model was most effective in the frequency range of 30 to 500 MHz and the high frequency model was used from 0.5 to 18.0 GHz. The low frequency model is similar to that used by Kuester, et. al. [9], in that a ray tracing model was used

and a similar RAM model was used. However, a uniform layer at the base of the RAM and a concrete dielectric layer under the floor RAM was added in this project. Other differences include the addition of the twisted pyramid RAM on the floor, and the output data format of a spatial, cylindrical scan instead of the site attenuation frequency scan in [9]. The high frequency model was similar to the chamber model in [12] and [13] in that ray tracing was used and the bistatic reflection derivation is the same. The bistatic pyramidal RAM tip diffraction, reflection coefficient subroutine in the file TIPBIST.FOR¹ from CHAMBER¹ was linked and adapted to the high frequency model. The high frequency chamber simulation differs from CHAMBER as follows: The was developed for a small compact range model whereas this project was adapted to a large rectangular chamber. Time gating was not used in this project as in CHAMBER. The chamber was not symmetric in all cases in this project whereas symmetry was used to reduce the number of computations in CHAMBER. The application configuration was bistatic in this project instead of monostatic. The RAM patch configuration differs slightly, also.

A verification of the effectiveness of the chamber simulation was conducted by comparing the simulation with measurements performed in the chamber by a cylindrical field probe scan. The verification was conducted at 300 MHz for the low frequency model and 10 GHz for the high frequency model. Differences in the simulation and measurements were resolved by processing the measured data by a cylindrical mode expansion to determine the angle of chamber scattering. The cylindrical mode expansion method was similar to that used by Bennet, et.al. [26] which was applied to data collected on an outdoor range.

The following section will describe the anechoic chamber geometry. The differences between the low and high frequency model will first be explained, followed by the RAM geometry, and then the

¹Joseph, P., "A UTD Scattering of Pyramidal Absorber for Design of Compact Range Chambers", Ph.D. Dissertation, OSU, 1988.

wall, ceiling and floor geometry.

1. CHAMBER MODEL GEOMETRY

The computer simulation project was developed to support a rectangular anechoic chamber with a 80 ft. diameter turntable located on the floor with the main coordinate system positioned at the center of the chamber turntable. The application of the simulation was for a large rectangular chamber (figure 2) with internal dimensions of 70 feet high, 250 feet wide and 265 feet long with an 80 foot diameter turntable. Pyramidal RAM covers all of the wall, floor and ceiling of the chamber with 18 inch long pyramids used in all cases except for the floor which was 48 inch long. The east and west walls of the chamber was located on the $y = -125$ and $y = 125$ ft. planes, respectively. The floor and ceiling are located on the $z = 0$ and $z = 70$ ft. planes, respectively. The back wall was located on the $x = -109.2$ ft. plane.

The probe antenna was located on the turntable (figure 3) and was scanned in the $+\phi_T$ direction. Figure 4 defines \vec{R}_A , \vec{R}_d , and \vec{r} . The range antenna location was given by equation (1). A cylindrical scan was formed when the probe location radial dimension was held constant as the height was varied. The direct path between the two antennas is given by equation (2). The cylindrical scan is given in equation (3).

$$\vec{R}_A = A_x \hat{x} + A_y \hat{y} + A_z \hat{z} \quad (1)$$

$$\vec{R}_d = \vec{r} - \vec{R}_A \quad (2)$$

$$\vec{r} = |r| \cos \phi_T \hat{x} + |r| \sin \phi_T \hat{y} + h \hat{z} \quad (3)$$

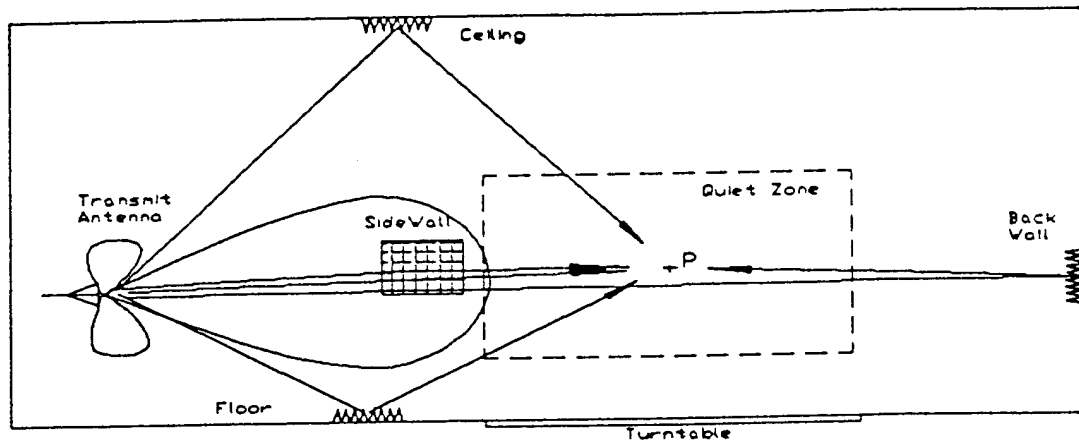


Figure 1 Anechoic Chamber Configuration Showing Multipath Effects in the Quiet Zone

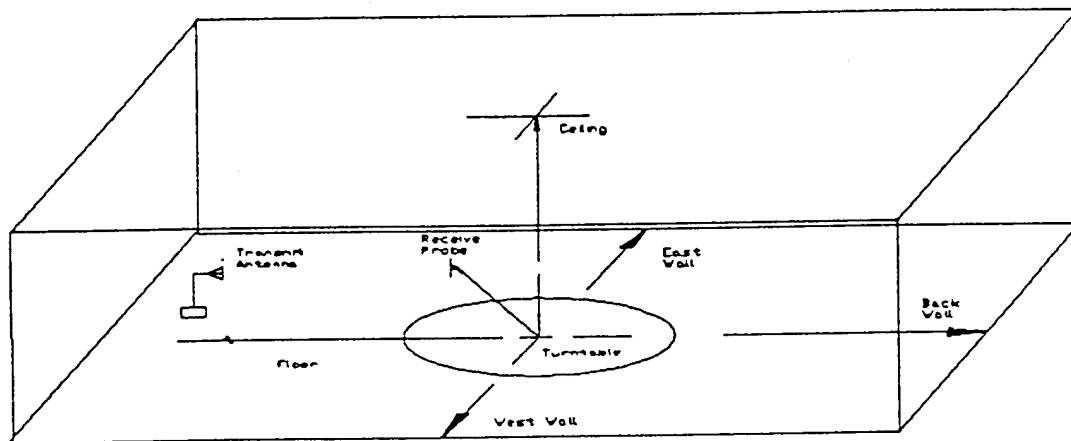


Figure 2 Wall Geometry

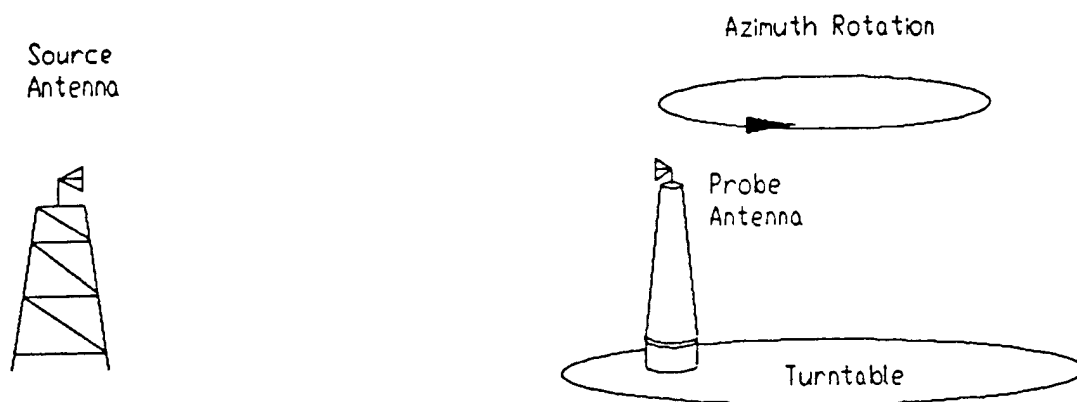


Figure 3 Cylindrical Scan

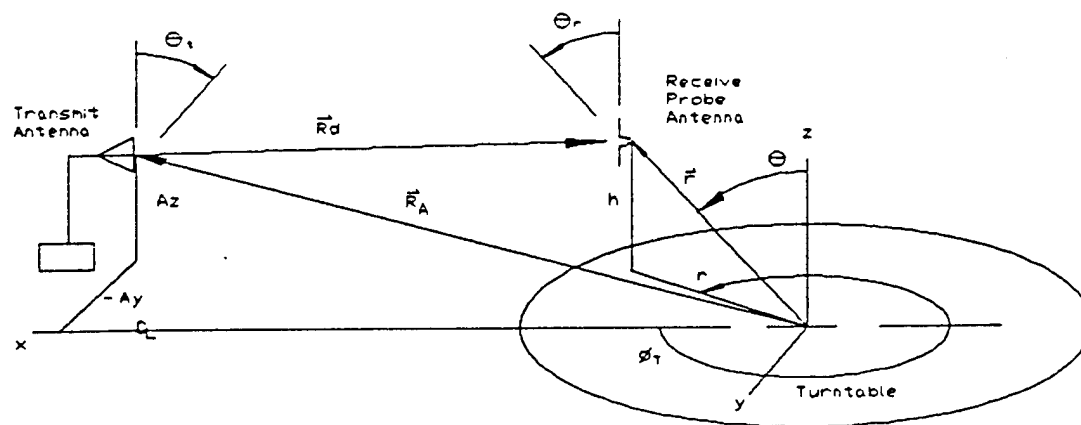


Figure 4 Cylindrical Scan Geometry

A. Low Frequency and High Frequency Model Geometry Contrast The wall, floor and ceiling multipath interaction configuration will differ in the modeling of the low frequency characteristics and the high frequency characteristics. The electromagnetic differences will be the subject of a later section of this report. The vector geometry differences between the low and high frequency model will be discussed here and then the application to each wall, floor or ceiling will be described.

The low frequency model was an approximation of the attenuation of the specular reflection (figure 5) since near the low end of the frequency spectrum, 30 MHz, the length of the RAM was much less than a wavelength. This implies there was one vector to each wall, floor or ceiling per scan point from the range antenna to the coordinates of the wall, floor or ceiling, and one vector from the conducting wall, floor or ceiling to the scanning probe. The method of images [27,28] (figure 6) will facilitate the configuration so that the two vectors are combined into one vector from the range antenna image to the probe antenna. Since the RAM was modeled as a bistatic reflection coefficient, by Snell's law of reflections [27] ($\Theta_{inc} = \Theta_{ref}$), the reflection and material refraction are symmetric, and the image ray vectors will trace a straight line from image to probe. The E-Field formulation of the multipath will include a consideration for the effects of the bistatic reflection coefficient, image boundary conditions, and spherical wave spreading. The incident angle between the negative of the incident wave vector and the normal vector from the coordinates of the walls, floor or ceiling was computed by the general equation in (4),

$$\vec{A} \cdot \vec{B} = |\vec{A}| |\vec{B}| \cos \theta = A_x B_x + A_y B_y + A_z B_z \quad (4)$$

where A and B are arbitrary vectors and θ is the angle between the vectors. The incident angle was then introduced into the low frequency model.

The high frequency model was concentrated entirely to the tips of the pyramidal RAM (figure 7) where a non-specular scattering is dominant to the specular scattering. The specular component

of the field was shown by Joseph in [13] to be attenuated enough to be neglected at high frequencies.

It was also shown by Joseph in [13] that each tip of the RAM will contribute to the total scattering in a random fashion so that the phase information of each tip scattering will be lost. He defined a patch of pyramids and the scattering component of each tip was summed for a total scattering component for each wall, floor and ceiling of the chamber. The concept of the random nature of the phase was used in this project when sufficient computer memory could not be allocated to include the entire wall of the chamber. The computer simulation of the scan was designed to accommodate large scan radii, which required large areas of the chamber to be modeled. Therefore, in lieu of defining an exact location of each pyramid tip, a new patch was defined for each scan angle. The new patch was centered at the specular location of the scan. Each patch of RAM surrounding the specular point was made as large as the mainframe computer would allow. At each scan angle, the E-field phasor from each tip was then added. From the random nature of the phase from each tip, it follows that the error introduced by this method was kept to a minimum.

The procedure for defining a typical patch (figure 8) is as follows: A vector from the range antenna was considered to be incident at a specular location at the tip of a pyramid which was at the center of the patch. The size of the M x N patch was specified in odd numbers. The surrounding pyramids in the patch was oriented around the center patch by the relationship in equations (5) and (6),

$$x_j = -\frac{(M-1)}{2} \cdot a + a \cdot (j-1) \quad (5)$$

$$y_k = -\frac{(N-1)}{2} \cdot a + a \cdot (k-1) \quad (6)$$

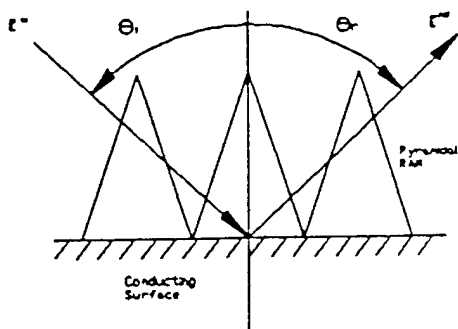


Figure 5 Specular Reflection Through Pyramidal RAM

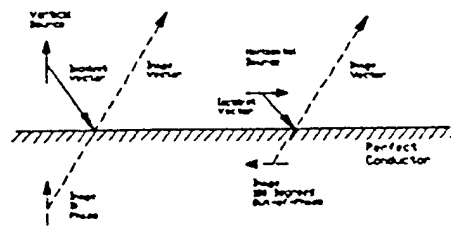


Figure 6 Method of Images

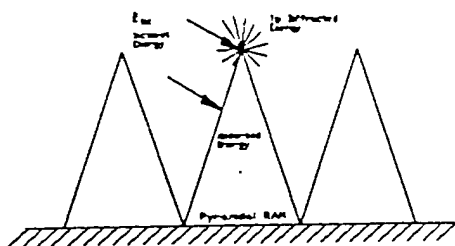


Figure 7 Dominant Tip Diffraction for High Frequency Model

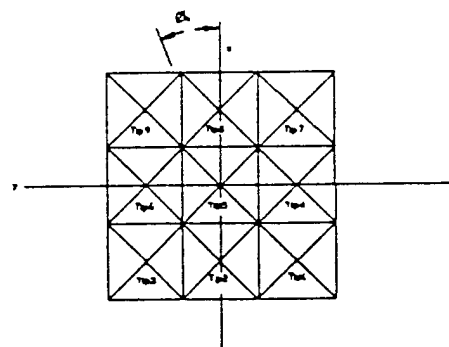


Figure 8 RAM Patch Top View Showing Local Coordinate System of Tip 5

where $i = 1$ to M , $j = 1$ to N , and a is the spacing between the RAM tips for the patch. A cartesian coordinate system was defined for each RAM tip with the z -axis along a unit normal vector from the coordinates of the wall, floor or ceiling. The x and y axes was defined for each wall, floor or ceiling. An incident theta and phi angle, Θ_{inc} and ϕ_{inc} respectfully (figure 9), was defined for each RAM tip by the dot product relation in equation (4) and the inverse tangent for the appropriate vectors. A scattering vector will then be defined from the tip of each RAM pyramid to the receive probe. A scattered theta and phi angle, Θ_{scat} and ϕ_{scat} respectfully, was defined in a similar manner to the incident angles. These angles will then be inputs to the BISTATIC subroutine [13] in the TIPBIST file [13].

The exception to the RAM patch method in the high frequency model was the back wall. The incident angles are always near the normal direction in the chamber configuration for the cylindrical scan. The bistatic scattering model will not be appropriate for this wall so an alternative method was used. A specular incident and scattering vector was defined at the conducting wall for each turntable angle similar to the low frequency model. However, manufacturer supplied data for the RAM was used for the reflection coefficient.

B. RAM Models As stated above, the chamber verification was in a chamber with 24 inch pyramid absorber on the walls, and ceiling. The exception was the floor where 48 inch pyramidal absorber was placed. Each pyramid absorber has a uniform base section and the floor has an intermediate layer of concrete that was seven inches thick before the conducting shield was encountered. The floor RAM type was a twisted pyramid RAM which causes the coordinate system at the tips to be shifted by 45 degrees.

The geometry of the low frequency RAM model is shown in figures 10 and 11. The total height of the RAM is L . It consists of a tapered, pyramidal section of length LB and a uniform section at the

base of thickness $L - L_B$. The layer of concrete shown in figure 10 was unique to the floor multipath, otherwise, the other walls, and ceiling will have the pyramid connected directly to the conductor. The spacing between RAM tips was a , and the width of the pyramid was a function of height, $d(z)$.

The geometry of the high frequency model for typical pyramid RAM tip was shown in figure 9. The details of how the geometry of the pyramid RAM was adapted to the UTD for dielectric corners, is given in [13] and the in-depth discussions are left for the interested reader. However, a brief description will be given as follows: A local coordinate system for each edge was defined with a corner for each edge at the apex of the pyramid. By the principle of superposition [28], the electric field contribution from each corner diffraction can be added to obtain the total scattering for each tip. The angle, α , of the RAM face is entered into the subroutine GEOMETRY in the TIPBIST subroutine which computes the local coordinate system of each of the four edges and the unit vectors needed to define the wedge/corner diffraction coordinates, the local polarization transform and the dielectric reflection/transmission coefficients. The unit vectors are transferred to BISTATIC through common variable statements. The exception to the geometry, as mentioned previously, was the twisted, pyramid RAM as shown in figure 12, where the upper portion of the pyramid was oriented at $\phi_0 = 45^\circ$ to the base where the tip coordinate system was defined.

C. Geometry of the Walls, Floor and Ceiling The geometry of every wall, floor and ceiling follows a similar format, so the floor geometry was derived in detail and the figures for the other walls, and ceiling can be used to visualize the relationships for that location. The floor geometry is shown in figure 13. The source antenna image is located by equation (7) and the vector from the image to the probe is given by equation (8). The specular angle at the base of the RAM is given in equation (9). The vector to the base of the RAM pyramid is found in equation (10) which makes use of the tangent formula in equations (11) and (12),

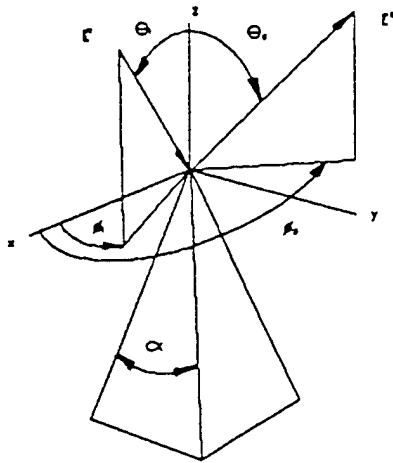


Figure 9 High Frequency RAM Tip Coordinate System

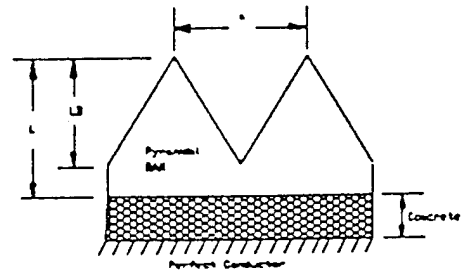


Figure 10 RAM Dimensions for Low Frequency Model

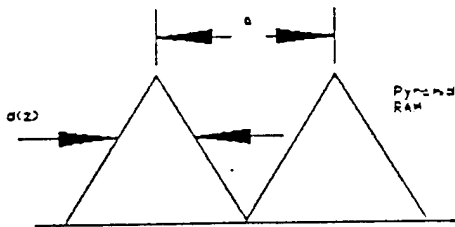


Figure 11 Taper Geometry for Low Frequency Model

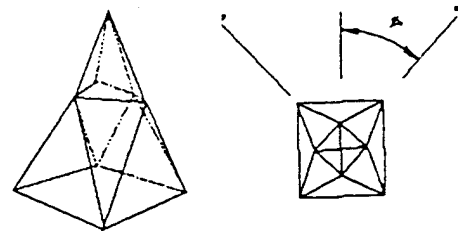


Figure 12 Twisted RAM Geometry

$$\vec{R}_{IF} = A_x \hat{x} + A_y \hat{y} - A_z \hat{z} \quad (7)$$

$$\vec{R}_F = \vec{r} + \vec{R}_{IF} \quad (8)$$

$$\theta_f = \cos^{-1} \left(\frac{\vec{R}_F \cdot \hat{z}}{|\vec{R}_F| |\hat{z}|} \right) \quad (9)$$

$$\vec{R}_{SF} = \vec{R}_{IF} + \vec{R}'_P \quad (10)$$

$$\tan \alpha_x = \frac{R_{Fz}}{R_{Fx}} = \frac{R'_{Fz}}{R'_{Fx}} \quad (11)$$

$$\tan \alpha_y = \frac{R_{Fz}}{R_{Fy}} = \frac{R'_{Fz}}{R'_{Fy}} \quad (12)$$

where α_x is the angle between the vector in equation (10) when projected on the $y = 0$ plane and the negative x-axis, and α_y is the angle between the vector in equation (10) when projected on the $x = 0$ plane and the y-axis.

The vector from the transmit horn to the RAM tip is given by equation (13),

$$\vec{R}_{TFT} = \vec{R}_{TF} - \vec{R}_A + x_j \hat{x} + y_k \hat{y} \quad (13)$$

$$\vec{R}_{TF} = \vec{R}_{RF} + \vec{R}_{SF} = L_F \hat{z} + \vec{R}_{SF} \quad (14)$$

and the vector from the RAM tip to the receive probe is given by equation (15).

$$\vec{R}_{TFS} = \vec{r} - \vec{R}_{TF} + x_j \hat{x} + y_k \hat{y} \quad (15)$$

Now, the incident and scattered angles at the tips are found from equations (16) through (19), which

was entered into BISTATIC.

$$\theta_{iF_{jk}} = \cos^{-1} \left(\frac{-\vec{R}_{TFT_{jk}} \cdot \hat{z}}{|\vec{R}_{TFT_{jk}}| |\hat{z}|} \right) \quad (16)$$

$$\phi_{iF_{jk}} = \tan^{-1} \left(\frac{-R_{TFTy_{jk}}}{-R_{TFTx_{jk}}} \right) \quad (17)$$

$$\theta_{SF_{jk}} = \cos^{-1} \left(\frac{\vec{R}_{TFS_{jk}} \cdot \hat{z}}{|\vec{R}_{TFS_{jk}}| |\hat{z}|} \right) \quad (18)$$

$$\phi_{SF_{jk}} = \tan^{-1} \left(\frac{R_{TFSy_{jk}}}{R_{TFSx_{jk}}} \right) \quad (19)$$

As stated above, the figures for the other walls, and ceiling can be used to visualize the similar relationships for the other walls, and ceiling. See figure 14 for the east wall, figure 15 for the west wall, figure 16 for the ceiling and figure 17 for the back wall. The figures show the appropriate coordinate system transformation relative for each wall and ceiling. The vector notation is consistent throughout so that a change in subscripts is sufficient to derive the entire set.

The next sections will describe the low and high frequency simulations in detail. The flow of the electromagnetic propagation will be described along with more detailed description of the RAM modeling mathematics. Computer resources, file management and polarization effects will also be discussed.

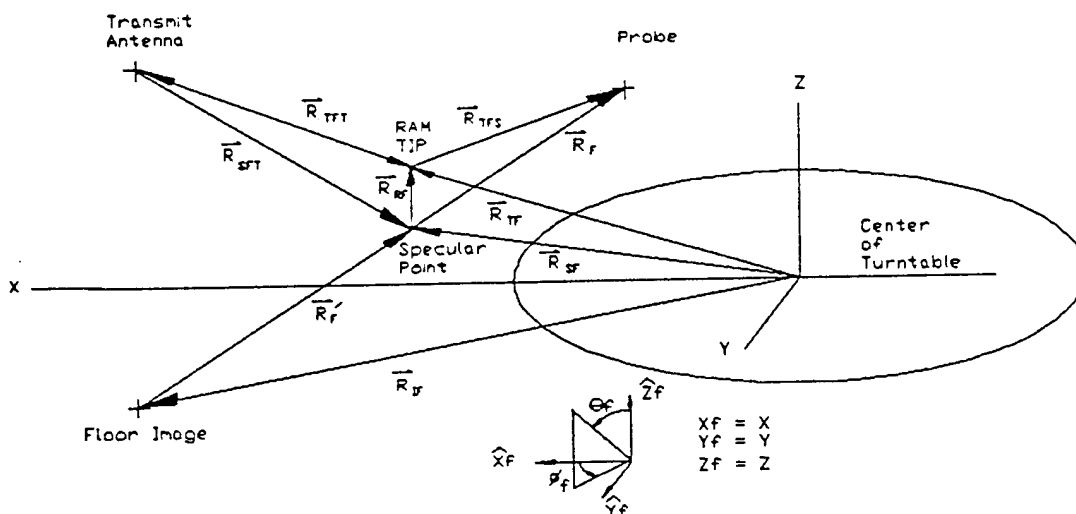


Figure 13 Floor Geometry

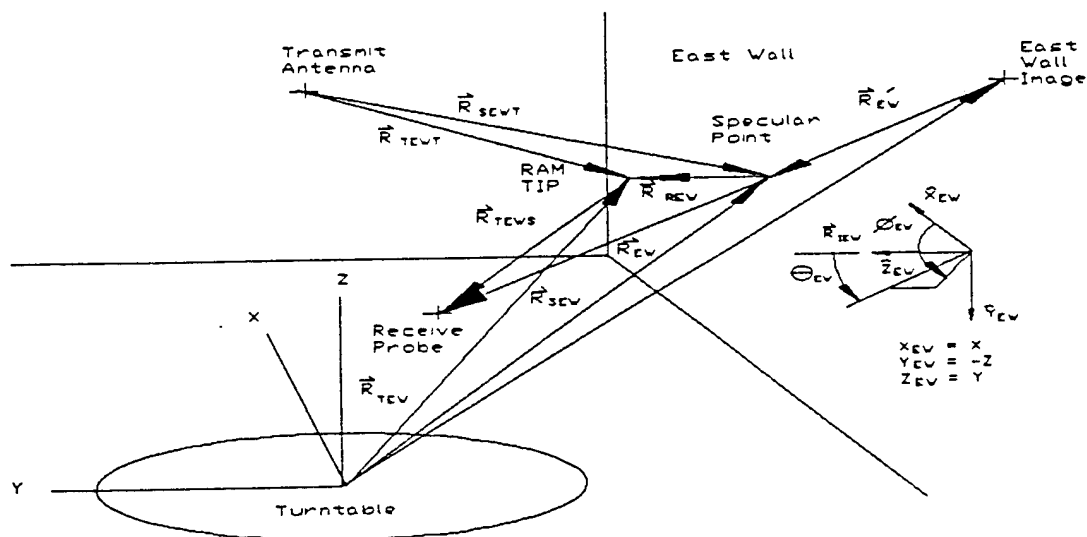


Figure 14 East Wall Geometry

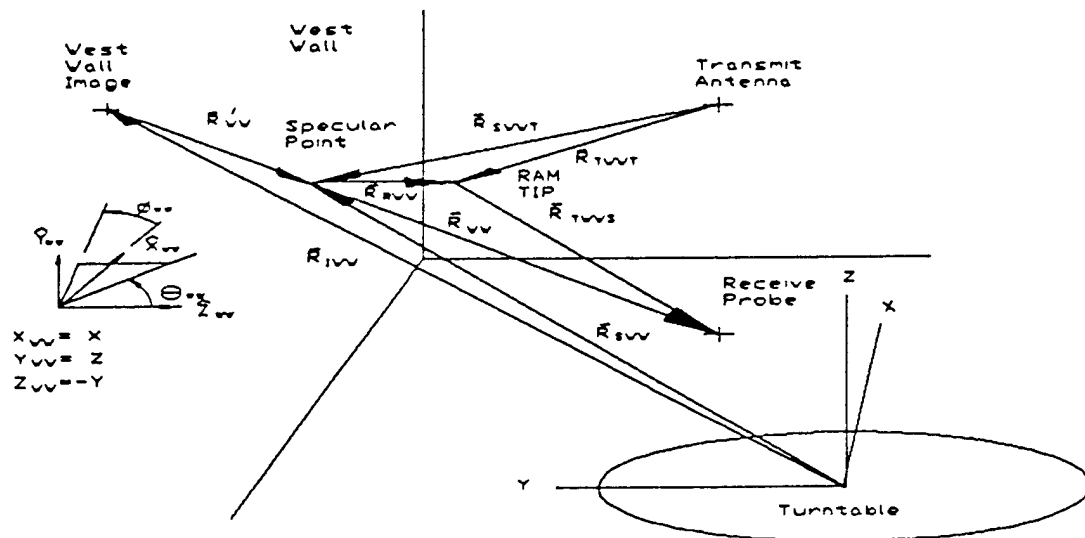


Figure 15 West Wall Geometry

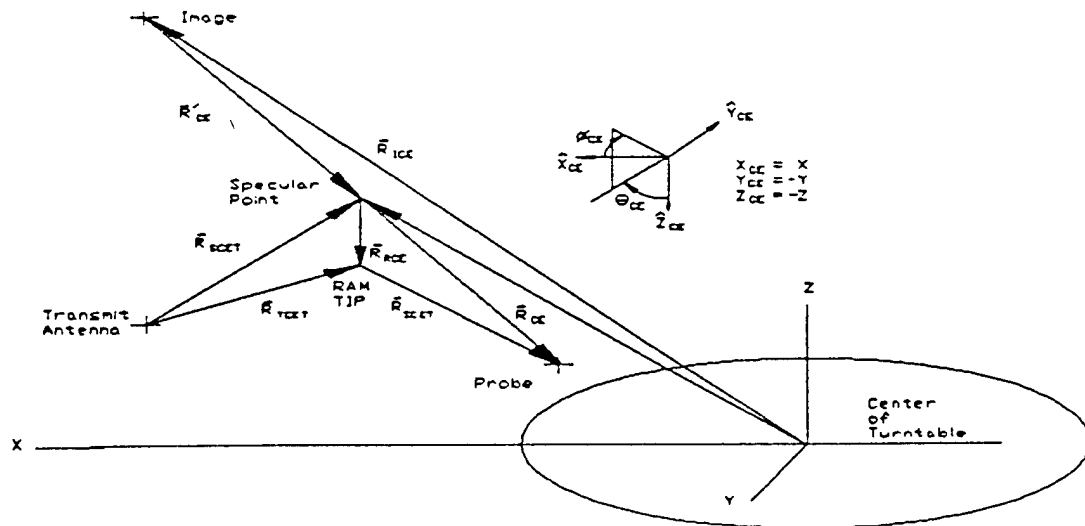


Figure 16 Ceiling Geometry

2. LOW FREQUENCY SIMULATION

The low frequency model consists of mathematical descriptions of the electromagnetic propagation in the chamber. An assumption was made that the dominant scatterer was the specular reflection from the walls so that multiple reflections and other objects in the chamber will not be included in the simulation.

The flow of the propagating wave occurs in the following manner. A stationary, dipole antenna transmits to a scanning receive dipole, probe antenna in the anechoic chamber and the specular reflections from the walls, floor and ceiling of the chamber. The transmitted waveform has a spherical wave spreading and phase factor given by the Green's function in equation (20),

$$\Psi = \frac{e^{-jkR}}{R} \quad (20)$$

where R is the distance from the range antenna and k is the free space wave number, $2\pi/\lambda$. A ray emanates from the range antenna directly to the receive probe and also from the range antenna in the direction of the specular reflection on the walls, floor and ceiling for each ϕ angle. Each ray was multiplied by the gain and normalized pattern factor of the range antenna. The distance of the specular paths was the distance from the image source to the receive probe. Each specular field component was multiplied by an attenuation factor or reflection coefficient caused by the RAM on the wall. The angle of incidence and polarization with respect to the plane of incidence of the ray must be considered to compute each reflection coefficient. The E-field phasors are then summed at the scan location and converted to power density by the relationship in equation (21),

$$S = \frac{|E|^2}{\eta} \quad (21)$$

where η is the free space impedance of 120π ohms, and then plotted in dBm/(sq ft) versus scan

angle. The angle of incidence for each ray to the receive probe was then used to compute the receive antenna pattern. Each ray E-field was multiplied by the receive pattern factor and again summed, converted to power density, and then to received power by the relationships in equation (22),

$$P_r = S \cdot A_{eff} = S \cdot \frac{G_r \lambda^2}{4\pi} \quad (22)$$

where A_{eff} is the effective aperture area, λ is the free space wavelength, and G_r is the receive antenna gain. The received power is then plotted in dBm versus scan angle.

A. RAM Model The low frequency RAM characteristics viz. the bistatic reflection coefficient used for the specular ray attenuation was calculated as follows: Since the length of a pyramid was small in terms of wavelength at the low frequencies, the RAM may be modeled as a rough layer of dielectric material with complex permittivity with periodic perturbations. The layer of RAM will have a tapered characteristic impedance much like a tapered impedance TEM transmission line with a load impedance, a short circuit in most instances. The details of the derivation of the reflection coefficient can be found in [23]-[25], and will be described briefly here without proof. The constituent properties of the material are modeled as an inhomogeneous, uniaxially anisotropic absorbing dielectric. The dielectric and permittivity constants will be in a tensor format as in matrix equations (23) and (24).

$$\hat{\epsilon} = \begin{bmatrix} \epsilon_x & 0 & 0 \\ 0 & \epsilon_y & 0 \\ 0 & 0 & \epsilon_z \end{bmatrix} \quad (23)$$

$$\hat{\mu} = \begin{bmatrix} \mu_x & 0 & 0 \\ 0 & \mu_y & 0 \\ 0 & 0 & \mu_z \end{bmatrix} \quad (24)$$

The RAM pyramids may be modeled as a periodic array of rods of spacing a (figure 18) that become tapered to form a pyramid. The relative volume of space occupied by the pyramid at a cross section in the z plane is given by $g = d(z)/a$. When a becomes small in terms of wavelengths, the material properties can be modeled by equations (25) through (28),

$$\epsilon_z = (1-g^2)\epsilon_o + g^2\epsilon_a \quad (25)$$

$$\mu_z = (1-g^2)\mu_o + g^2\mu_a \quad (26)$$

$$\epsilon_x = \epsilon_y = \epsilon_o \left[1 + g^2 \frac{2(\epsilon_a - \epsilon_o)}{(1+g^2)\epsilon_o + (1-g^2)\epsilon_a} \right] \quad (27)$$

$$\mu_x = \mu_y = \mu_o \left[1 + g^2 \frac{2(\mu_a - \mu_o)}{(1+g^2)\mu_o + (1-g^2)\mu_a} \right] \quad (28)$$

where ϵ_a and μ_a are the relative permittivity and permeability parameters, respectively, and ϵ_o and μ_o are the permittivity and permeability of free space, respectively. It is assumed that all of the materials used are non-ferrous, so $\mu_a = \mu_o$. For an E-field that is perpendicular to the plane of incidence the effective material properties are given in equations (29) and (30),

$$\epsilon_{eff} = \epsilon_y - \frac{\epsilon_o \mu_o \sin^2 \theta}{\mu_z} \quad (29)$$

$$\mu_{eff} = \mu_x \quad (30)$$

and in equations (31) and (32) for an E-field that is parallel to the plane of incidence.

$$\epsilon_{eff} = \epsilon_x \quad (31)$$

$$\mu_{eff} = \mu_y - \frac{\epsilon_o \mu_o \sin^2 \theta}{\epsilon_z} \quad (32)$$

The equivalent TEM transmission line parameters of the characteristic impedance, $Z_c(z)$, and the propagation constant, $\gamma(z)$, are given by equations (33) and (34).

$$Z_c(z) = \sqrt{\frac{\mu_{eff}(z)}{\epsilon_{eff}(z)}} \quad (33)$$

$$\gamma(z) = j\omega \sqrt{\mu_{eff}(z) \epsilon_{eff}(z)} \quad (34)$$

It was assumed that the reflection coefficient was small enough that smaller order terms can be neglected [32], the reflection coefficient from a typical wall is given by equation (35),

$$\Gamma(0) = \Gamma_1(0) + \Gamma_2(0) \quad (35)$$

where

$$\Gamma_1(0) = e^{-2 \int_0^L \gamma(z') dz'} \Gamma_L \quad (36)$$

$$\Gamma_2(0) = \int_0^{L-LB} N(z') e^{-2 \int_0^{z'} \gamma(z'') dz''} dz' \quad (37)$$

$$N(z) = \frac{\frac{\partial}{\partial z} Z_c(z)}{2 Z_c(z)} \quad (38)$$

and $\Gamma_L = -1$. Since the material was continuous between the pyramid tapered layer and the

uniform bottom layer, the reflection coefficient was assumed to be zero.

The floor has an intermediate concrete layer with thickness d_{con} and was modeled by equation (39),

$$\Gamma_F(0) = \Gamma_{F1}(0) + \Gamma_{F2}(0) + \Gamma_{F3}(0) \quad (39)$$

where,

$$\Gamma_{F1}(0) = e^{-2\int_0^L \gamma(z') dz'} \Gamma_{con} \quad (40)$$

$$\Gamma_{con} = \frac{\eta_{con} - \eta_{abs}}{\eta_{con} + \eta_{abs}} \quad (41)$$

$$\eta_{con} = \sqrt{\frac{\hat{\mu}_{con}}{\hat{\epsilon}_{con}}} \quad (42)$$

$$\Gamma_{F2}(0) = \Gamma_1(0) \quad (43)$$

$$\Gamma_{F3}(0) = \Gamma_L e^{-2[\gamma_2 d_{con} + \int_0^L \gamma(z') dz']} \quad (44)$$

$$\gamma_2 = j\omega\sqrt{\epsilon_{con}\mu_{con}} \quad (45)$$

multiple reflections are neglected between layers since the reflections are small, and $\eta_{con} = \eta_o$ and $\epsilon_{con} = 10\epsilon_o$ are assumed as the constituent properties of the concrete layer [33], where the permittivity has been estimated based on the permittivities of the concrete materials. The reflection between the pyramidal and uniform layer are again assumed to be zero.

B. Computer Resources The simulation has been developed on a Z486 PC and uses a MATHCAD[®]

version 3.0 software package [34]. Since a single file will contain a maximum of 50 variables, which decreases as the number of iterations or integrals increases, several files were cascaded to complete the computation. The files were connected by WRITE and READ statements which passed the relevant arrays between files. A total of 26 files were used in the low frequency model, and the flow chart of figure 19 shows the order of the files. A check was added to the beginning of each file to assure the order was maintained and a statement of where to go next was placed at the end of each file for convenience.

The integrals evaluated in the RAM model in MATHCAD® use a numerical algorithm called a Romberg integration. The lower limit of the reflection coefficient integral had to be offset slightly from zero to avoid a convergence problem with the algorithm.

C. Polarization and Orientation Considerations The polarization for the low frequency simulation was vertical to the chamber floor. The propagating E-field was represented in polar coordinates as E_θ . The floor polarization remains the same throughout. The ceiling orientation of the E-field was E_θ when referenced to the local coordinate system. The east and west wall E-field orientation were E_ϕ and E_ϕ respectfully for the local coordinate system. The east, west and back walls have a 180 degree, boundary value, phase shift in the low frequency model consistent with image theory.

The reflection coefficient for each polarization component was referenced to the plane of incidence. The floor and ceiling E-field consistently has only a component that was parallel to the plane of incidence (figure 20). However, the east, west and back wall each have a parallel and perpendicular component. The derivation for the components of the east wall will be shown here. The components for the other walls were derived and used in a similar manner. Figure 21 shows the field orientation and the plane of incidence referenced to the east wall. The unit vectors along the direction of propagation with respect to the plane of incidence are given by equations (46) and (47).

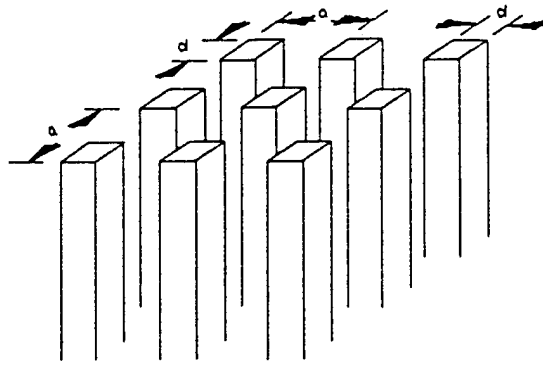


Figure 18 Transverse, Periodic, Rectangular, Lossy Rods Used in Low Frequency Formulation

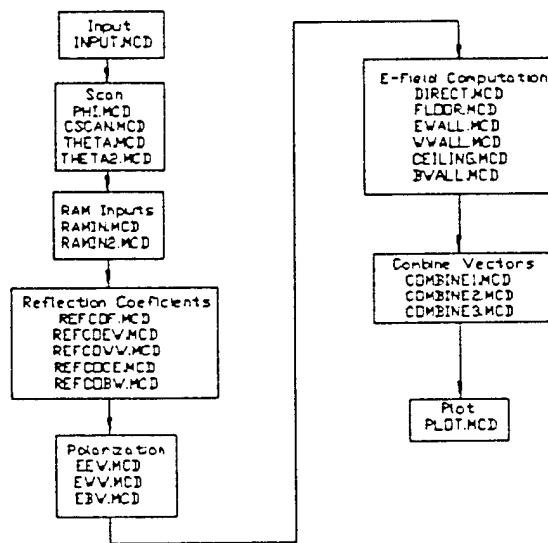


Figure 19 Flow Chart for Low Frequency Model

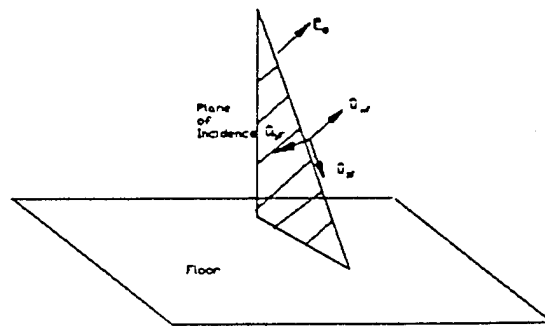


Figure 20 Floor Polarization Orientation

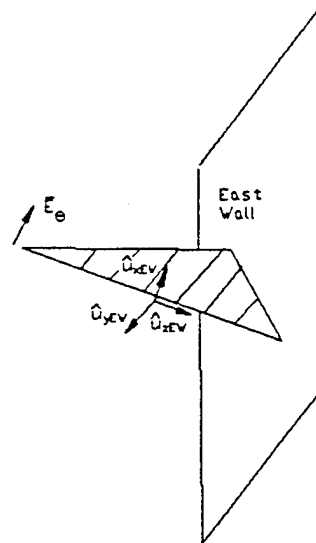


Figure 21 East Wall Polarization Orientation

$$\hat{u}_{x_{EW}} = \frac{\vec{R}_{SEWT} \times (-\hat{y})}{|\vec{R}_{SEWT}|} \quad (46)$$

$$\hat{u}_{y_{EW}} = \frac{\vec{R}_{SEWT} \times \hat{u}_{x_{EW}}}{|\vec{R}_{SEWT}|} \quad (47)$$

The E-field was converted to rectangular coordinates by multiplication by the vector in equation (48).

$$\begin{aligned} \vec{E}_{EW} &= E_{\theta} \cdot \hat{u}_{polar} \\ &= E_{\theta} \cdot (\cos\theta_{SEWT} \cos\phi_{SEWT} \hat{x} + \cos\theta_{SEWT} \sin\phi_{SEWT} \hat{y} - \sin\theta_{SEWT} \hat{z}) \end{aligned} \quad (48)$$

The parallel and perpendicular components are then given by equations (49) and (50).

$$\vec{E}_1 = \vec{E}_{EW} \cdot \hat{u}_{y_{EW}} \quad (49)$$

$$\vec{E}_2 = \vec{E}_{EW} \cdot \hat{u}_{x_{EW}} \quad (50)$$

The parallel and perpendicular fields are then multiplied by the appropriate reflection coefficient and then summed.

D. Source and Receive Antennas A half-wave dipole oriented vertically or on the z-axis of the turntable coordinate system, was used for the source and receive antennas. A half-wave dipole has a directivity of 1.64 or 2.1 dBi [27,28] and has an omni-directional pattern in ϕ . Each ray in the

simulation was multiplied by a transmit normalized antenna pattern defined by the angle Θ of the ray. The receive ray was multiplied by the normalized dipole pattern if the received power was the displayed quantity. The elevation pattern for a typical half-wave dipole is given by equation (51).

$$PF_{dipole} = \frac{\cos\left(\frac{\pi}{2} \cos\theta\right)}{\sin\theta} \quad (51)$$

The derivation of the direct path and floor angles Θ_i and Θ_r is shown here. Equations for these angle for the other walls were derived in a similar manner. The angles for the direct path are given by equations (52) and (53),

$$\theta_{pdt} = \cos^{-1}\left(\frac{\vec{R}_d \cdot \hat{z}}{|\vec{R}_d| |\hat{z}|}\right) \quad (52)$$

$$\theta_{pdr} = \cos^{-1}\left(\frac{-\vec{R}_d \cdot \hat{z}}{|\vec{R}_d| |\hat{z}|}\right) \quad (53)$$

and the angles for the floor are given by equations (54) and (55).

$$\theta_{pft} = \cos^{-1}\left(\frac{\vec{R}_{sFT} \cdot \hat{z}}{|\vec{R}_{sFT}| |\hat{z}|}\right) \quad (54)$$

$$\theta_{pfr} = \cos^{-1}\left(\frac{-\vec{R}_F \cdot \hat{z}}{|\vec{R}_F| |\hat{z}|}\right) \quad (55)$$

E. Number of Data Points The number of data points in a scan was determined by the Nyquist criteria [26][35], and also by the FFT algorithm in the cylindrical wave expansion. For a cylindrical scan the maximum angle increment determined by the Nyquist criteria is given in equation (56),

$$\Delta\phi = \frac{\phi_1 - \phi_2}{N_{pts}} = \frac{\pi}{kR} = \frac{\lambda}{2R} \quad (56)$$

which for a 2π radian scan reduces to $kR \leq N_{ps}/2$. The FFT algorithm requires that the number of data points be a factor of $N = 2^n$, where n is an integer.

The high frequency model will be described next. The frequency range of the high frequency model will be applied was 500 MHz to 18 GHz. This model can also be applied to the low frequencies since the model assumes a pyramid of infinite length; but, since the specular reflection was so large at the lower frequencies, the diffraction effects became less significant.

3. HIGH FREQUENCY SIMULATION

The high frequency model was also a mathematical description of the propagation and scattering/multipath interference in a rectangular anechoic chamber. The overall format was the same as the low frequency model. The major differences are the way the RAM was modeled and the type of range antenna used. The RAM model assumes that the RAM tips are the dominant sources of scattering. Since there are many RAM tips, the number of GO rays that are modeled and summed are significantly increased compared to the low frequency model. For instance, a 20 x 20 RAM patch has 1602 rays versus a maximum of six rays in the low frequency model.

The power flow in the high frequency model was similar to the low frequency model except that image theory was not applied. This means that the phase shift will not occur since the scattering was coming from the tips and not the conducting wall. Also, the distances used in the spherical wave spreading attenuation was calculated from the vector from the range antenna to the RAM tips plus the vector from the RAM tips to the receive antenna. An assumption was also made that these two distance vectors are nearly equal when computing the reflection coefficient. The spherical wave spreading was added in this model because it was not included in the TIPBIST formulation in [13]. The diffraction model assumes that the incident and reflections are far enough away that a plane

wave assumption was made. Since only the relative value between the incident and scattered energy was used to compute the reflection coefficient, the input E-field was set to unity with the appropriate polarization and the reflection coefficient was computed from $E^{\text{scat}}/E^{\text{inc}}$.

A. RAM Model The input to the TIPBIST GEOMETRY subroutine wedge angle and the inputs to the BISTATIC subroutine are E_{θ}^{inc} , E_{ϕ}^{inc} , Θ^{inc} , Φ^{inc} , Θ^{scat} , and Φ^{scat} . These quantities were computed in the Geometry section of this report. The RAM model was a summation of four dielectric edges with a corner diffraction term for each edge at the apex of the pyramid. The four edges are modeled separately with a three dimensional, dielectric, UTD algorithm with the corner diffraction term added. The details of this algorithm are developed shown in reference [13], where the development of the various stages of the model was found. An overview of the relevant algorithm used in TIPBIST will be shown below with the same notation as that of reference [13]. The overall equation will be shown for one edge of the RAM and each component of the equation will be explained. Since a great deal of the formulation was spent in transforms between coordinate systems and in model interfaces (from models that were developed separately), the derivation shown here will be brief.

The overall equation for the scattered E-field in BISTATIC is given in equation (57).

$$\begin{bmatrix} E_{\beta_{oc}}^c \\ E_{\phi}^c \end{bmatrix} = \begin{bmatrix} C_a(Q_E) & C_b(Q_E) \\ C_c(Q_E) & C_d(Q_E) \end{bmatrix} \begin{bmatrix} E_{\beta_c}^i(Q_c) \\ E_{\phi_c}^i(Q_c) \end{bmatrix} \frac{e^{-j\frac{\pi}{4}}}{\sqrt{2\pi k}} \frac{\sqrt{\sin\beta_c \sin\beta_{oc}}}{(\cos\beta_{oc} - \cos\beta_c)} \quad (57)$$

in which,

$$C_a(Q_E) = \left\{ \begin{array}{l} (R_1 \cos^2 \alpha_n - R_1 \sin^2 \alpha_n) C_n(\phi + \phi') \\ + (R_1 \cos^2 \alpha_o - R_1 \sin^2 \alpha_o) C_o(\phi + \phi') \end{array} \right\} \quad (58)$$

$$C_b(Q_E) = \left\{ \begin{array}{l} (R_1 + R_1) [\sin \alpha_n \cos \alpha_n C_n(\phi + \phi') \\ + \sin \alpha_o \cos \alpha_o C_o(\phi + \phi')] \end{array} \right\} \quad (59)$$

$$C_c(Q_E) = \left\{ \begin{array}{l} -(R_1 + R_1) [\sin \alpha_n \cos \alpha_n C_n(\phi + \phi') \\ + \sin \alpha_o \cos \alpha_o C_o(\phi + \phi')] \end{array} \right\} \quad (60)$$

$$C_d(Q_E) = \left\{ \begin{array}{l} (R_1 \cos^2 \alpha_n - R_1 \sin^2 \alpha_n) C_n(\phi + \phi') \\ + (R_1 \cos^2 \alpha_o - R_1 \sin^2 \alpha_o) C_o(\phi + \phi') \end{array} \right\} \quad (61)$$

where,

$$C_o(\beta) = \frac{-e^{-j\frac{\pi}{4}}}{2n\sqrt{2\pi k} \sin \beta_o} \cot\left(\frac{\pi_+(\beta)}{2n}\right) F\left[\frac{L_{a+}(\beta)/\lambda}{kL_c a(\pi + \beta_{oc} - \beta_c)}\right] \quad (62)$$

$$\left(\frac{L}{L_c}\right)_m = \frac{\left(\frac{S'_m S''}{S'_m + S''}\right)}{\left(\frac{S_c S}{S_c + S}\right)} \sin^2 \beta_{om} \quad (63)$$

$$R_1 = \frac{\cos \theta^i - \sqrt{\left(\frac{\epsilon_2}{\epsilon_1}\right) - \sin^2 \theta^i}}{\cos \theta^i + \sqrt{\left(\frac{\epsilon_2}{\epsilon_1}\right) - \sin^2 \theta^i}} \quad (64)$$

$$R_1 = \frac{\left(\frac{\epsilon_2}{\epsilon_1}\right) \cos \theta^i - \sqrt{\left(\frac{\epsilon_2}{\epsilon_1}\right)}}{\left(\frac{\epsilon_2}{\epsilon_1}\right) \cos \theta^i + \sqrt{\left(\frac{\epsilon_2}{\epsilon_1}\right) - \sin^2 \theta^i}} \quad (65)$$

$$F(x) = 2j\sqrt{x} e^{jx} \int_{\sqrt{x}}^{\infty} e^{-j\tau^2} d\tau \quad (66)$$

$$a^{\pm}(\beta) = 2\cos^2 \left[\frac{2n\pi N^{\pm} - \beta}{2} \right] \quad (67)$$

and N^{\pm} are integers that are derived by rounding off the solutions of equation (68),

$$2\pi n N^{\pm} - \beta = \pm\pi \quad (68)$$

$$n = 2 - WA/\pi \quad (69)$$

Also, WA is the wedge angle, k is the wavenumber, ϵ_1 is the free space permittivity, ϵ_2 is the complex permittivity of the RAM material. The o subscript refers to the incident face of a wedge and n refers to the shadow face of the wedge. The function $F(x)$ is the transition function used in the standard UTD formulation; however, the ratio L/L_0 is considered constant in BISTATIC. The C_+ through C_- are the corner diffraction terms for four wedges, and, the R_1 and R_2 are the reflection coefficient terms used to account for the dielectric boundaries of the wedge. The parameters β , β_{oc} , β_c , and β_o are defined in figures 23 through 25.

B. Back Wall As mentioned in a previous section, the incident angle to the back wall was assumed to be always near normal incidence and was therefore modeled by manufacturer supplied data. The back wall attenuation for the RAM was specified as -50 dB. The free space attenuation for the back wall was significantly larger than the other walls, so the assumption will not affect the outcome of the results.

C. Computer Resources The high frequency model was programmed in Fortran on a VAX mainframe computer and linked with the TIPBIST file. A flow chart of the program is shown in figure 26. The amount of memory needed for the large arrays from the RAM patches necessitated a mainframe computer.

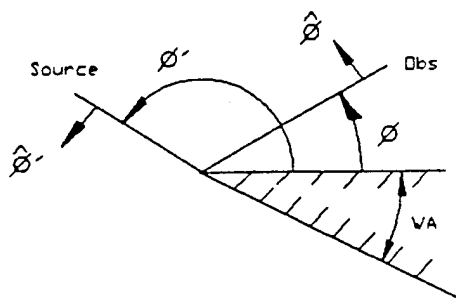


Figure 22 Side View of Wedge

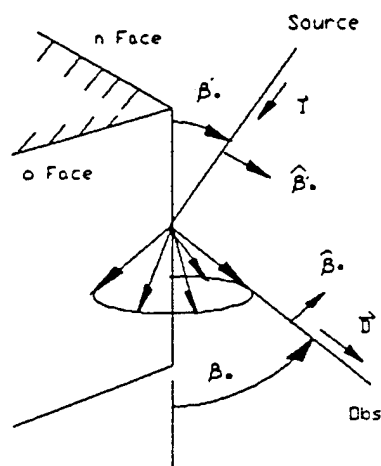


Figure 23 Oblique Incidence in Wedge

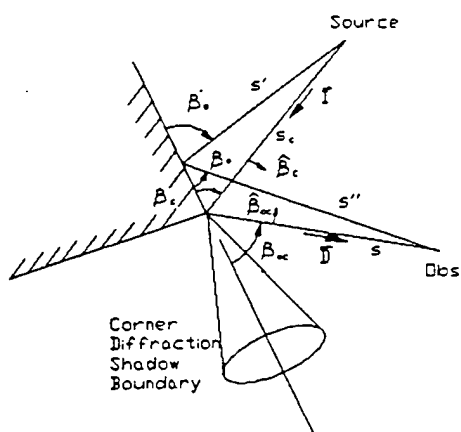


Figure 24 Corner Diffraction on a Wedge

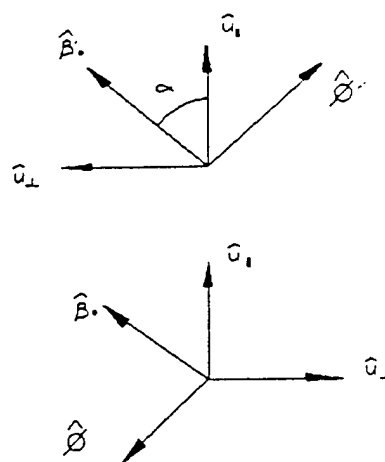


Figure 25 Polarization used on Wedge Corner Diffraction, Upper is Incident Orientation and Lower is Scattered Orientation.

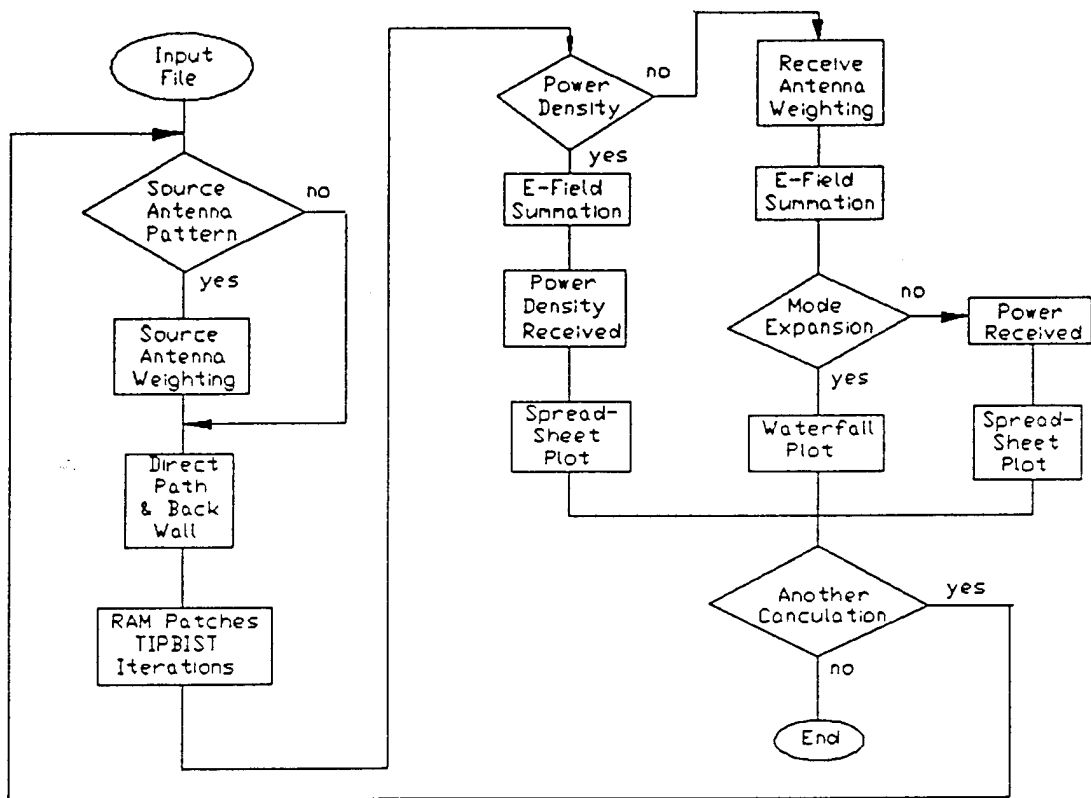


Figure 26 Flow Chart for High Frequency Model

D. Receive and Source Antenna The receive probe antenna was a half-wave dipole as in the low frequency model. The source antenna for the high frequency model was a TE₁₁ diagonal horn. The mathematical model for the radiation pattern was developed by Love [37]. The radiation pattern was symmetric in the principal planes though somewhat degraded in the intercardinal planes. The directivity of the horn was found with the equation $D_r = 4\pi A_{eff}/\lambda$ with an efficiency of 0.81. The mode structure in the aperture is shown in figure 27 and the local coordinate system is shown in figure 28. A coordinate transformation was necessary for each wall to the local coordinate system of the wall. The transformation will be shown for the direct path and the floor, whereas the formulation for the other walls was similar.

The E-field for the TE₀₁ and TE₁₀ modes are orthogonal/independent so that they may be calculated separately. The resultant field was then found from the combination. The E-field for each mode is given by equations (70) and (71).

$$E_y(\theta, \phi) = \frac{2d^2}{\pi} \frac{\sin(u \sin \phi)}{u \sin \phi} \frac{\cos(u \cos \phi)}{1 - \frac{4u^2}{\pi^2} \cos^2 \phi} \quad (70)$$

$$E_x(\theta, \phi) = \frac{2d^2}{\pi} \frac{\sin(u \cos \phi)}{u \cos \phi} \frac{\cos(u \sin \phi)}{1 - \frac{4u^2}{\pi^2} \sin^2 \phi} \quad (71)$$

where,

$$u = \frac{\pi d}{\lambda} \sin \theta \quad (72)$$

$$E_{DH} = \sqrt{E_x^2 + E_y^2} \quad (73)$$

and d is the length of the side of the square aperture. The coordinate transfer for the direct path

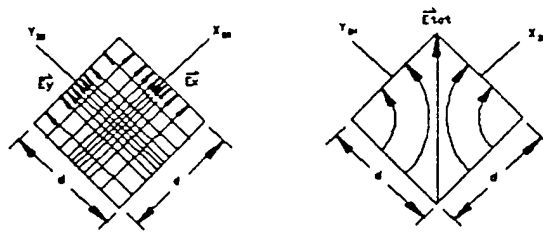


Figure 27 Diagonal Horn Modes

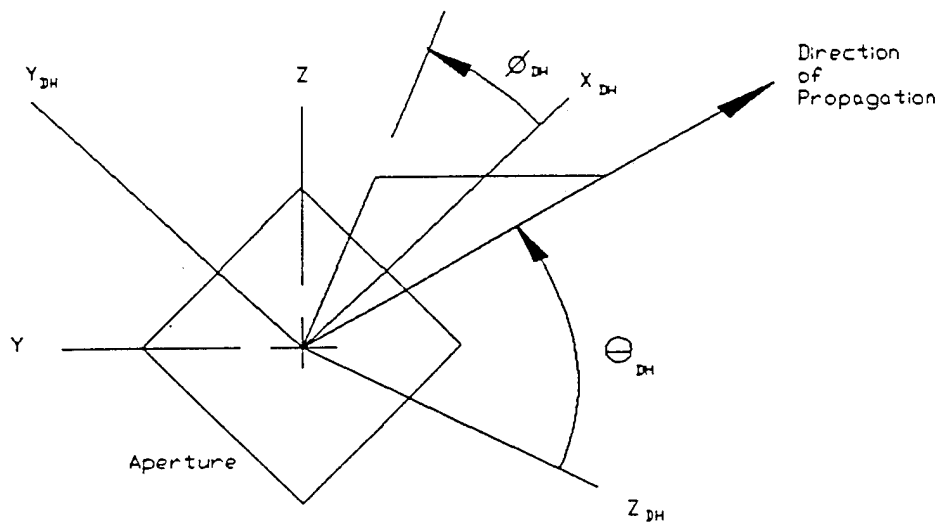


Figure 28 Diagonal Horn Antenna Coordinate System

is given in equations (74) through (76).

$$\begin{aligned} R_{dDH_z} &= -R_{d_x} \\ R_{dDH_y} &= (R_{d_y} + R_{d_z}) / \sqrt{2} \\ R_{dDH_x} &= (R_{d_z} - R_{d_y}) / \sqrt{2} \end{aligned} \quad (74)$$

$$\begin{aligned} \theta_{dDH} &= \cos^{-1} \left(\frac{R_{dDH_z}}{|\vec{R}_d|} \right) \\ \phi_{dDH} &= \cos^{-1} \left(\frac{R_{dDH_x}}{|\vec{R}_d| \sin \theta_{dDH}} \right) \end{aligned} \quad (75)$$

$$\begin{aligned} E_{d_\phi} &= E_{DH}(\theta_{dDH}, \phi_{dDH}) \\ E_{d_\theta} &= 0 \end{aligned} \quad (76)$$

The coordinate transfer for the floor path is given in equations (77) through (79).

$$\begin{aligned} \theta_{fDH} &= \cos^{-1} \left(\frac{R_{fDH_z}}{|\vec{R}_{TFT}|} \right) \\ \phi_{fDH} &= \cos^{-1} \left(\frac{R_{fDH_x}}{|\vec{R}_{TFT}| \sin \theta_{fDH}} \right) \end{aligned} \quad (77)$$

$$\begin{aligned} E_{f_\phi} &= E_{DH}(\theta_{fDH}, \phi_{fDH}) \\ E_{f_\theta} &= 0 \end{aligned} \quad (78)$$

$$\begin{aligned} R_{fDH_z} &= -R_{TFT_x} \\ R_{fDH_y} &= (R_{TFT_y} + R_{TFT_z}) / \sqrt{2} \\ R_{fDH_x} &= (R_{TFT_z} - R_{TFT_y}) / \sqrt{2} \end{aligned} \quad (79)$$

E. Number of Data Points The number of data points used the same criteria as the low frequency model.

4. MODAL EXPANSION PROCESSING

A modal expansion of the E-field can be used to determine the fields at any other radius than the measurement radius. The fields converge in phase when a radiating source was encountered, and can be used to locate scattering sources in the chamber. The methodology of the simulation and verification was to compare the predicted data to measured data. When a discrepancy was experienced, a modal expansion was performed on the measured data to determine where the scattering was coming from. It was hopeful that scattering sources other than the RAM covered walls can be located and corrected.

The modal expansion used was found in reference [26] and is given by equation (80),

$$E_z(r, \phi) = FFT^{-1} \left\{ \frac{FFT[E_z(R, \phi)]}{\sum_{n=-\infty}^{\infty} H_n^{(2)}(kR)} \sum_{n=-\infty}^{\infty} H_n^{(2)}(kr) \right\} \quad (80)$$

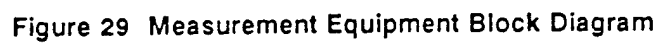
where R is the scan radius, $E_z(R, \phi)$ is the measured data, FFT is a Fast Fourier Transform, and $H_n^{(2)}$ is a Hankel function of the second kind. The distance resolution of the measurement was obtained by sweeping several frequencies around the center frequency. After the modal expansion, the frequency components of the electric field are added. The phasors of the field add when a source was encountered in the chamber and create a maximum in the field magnitude. When there were no prevalent scattering sources, the electric fields add in phase randomly and do not typically create any significant magnitude.

5. MEASUREMENT CONFIGURATION

The measurements were conducted in a rectangular chamber as described in the geometry section. An automatic vector network analyzer (Hewlett Packard HP8510) coherent detection system was used to receive and collect the data. A block diagram of the equipment is shown in figure 29. A Flam and Russell 959 system was used to process the data for an antenna pattern format and controlled the antenna positioning system. The 80 foot chamber turntable was not available during the measurements, so a Scientific Atlanta (SA) azimuth positioner was substituted for the measurement. The location of the positioner in the chamber is shown in figure 30. An arm constructed of low density wood was fabricated to provide the cylindrical scan (figure 31). The positioning equipment, wooden arm and input cable was covered with available RAM so that additional scattering would not interfere with the measurements. The RAM was placed to cover the input cable to the antennas as much as possible to prevent scattering from the cable from interfering with the measurements.

The antennas used for the simulation verification measurements were dipoles. A sleeve dipole tuned to 10 GHz was used for the high frequency measurements. The sleeve dipole was constructed of 0.141 coaxial cable with a brass sleeve choke to form the lower half of the dipole and suppress input cable currents. The dipoles for the low frequency measurements were from a calibrated EMCO Model 3121C Tuned Dipole Antenna set. The dipoles were tuned and measured (figure 32 and 33) with an HP8757 Scalar Network Analyzer.

The antenna used for the diagnostic measurements was a broadbeam horn. A TECOM Type No. 201187-4 Dual-Polarized, Quad-Ridge Horn was selected. The cross polarized port of the horn was terminated with a 50 ohm load. The beamwidth of the horn was 80° to 40°, which was similar to an open-ended waveguide. The horn antenna was substituted as close as possible to the exact location of the dipole at the top of the positioning arm. The horn fixture below the dipole location



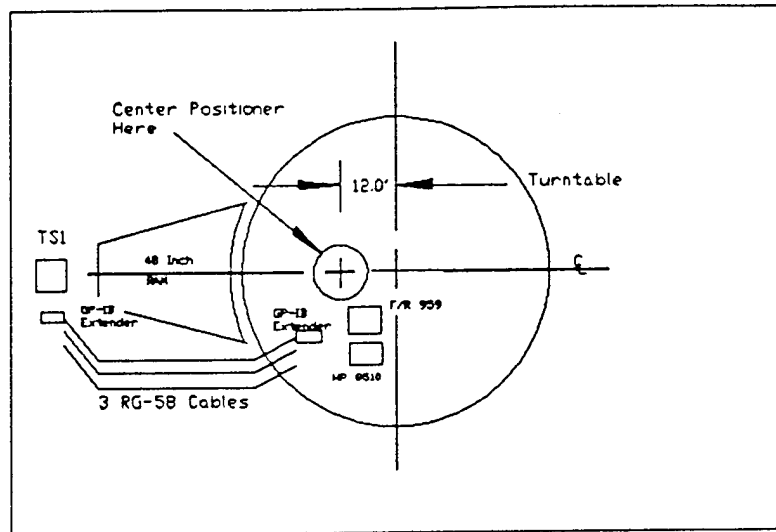


Figure 30 Location of the S/A Positioner in the Chamber

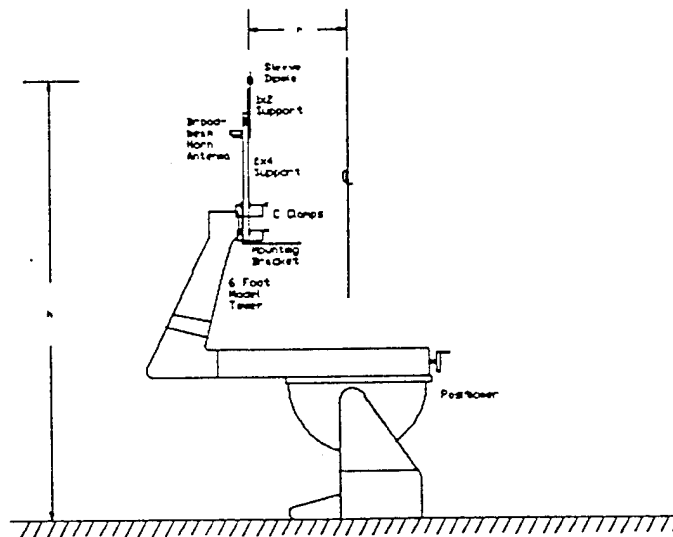


Figure 31 Positioner Configuration with Antenna Fixture

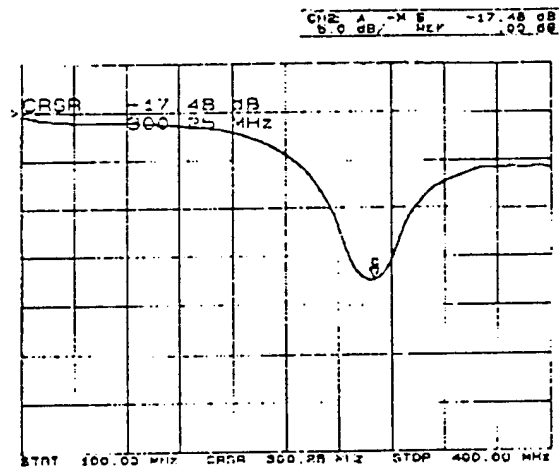


Figure 32 Low Frequency Dipole Antenna Tuning

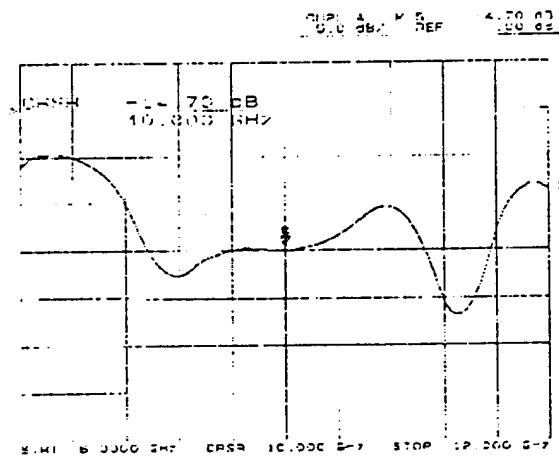


Figure 33 High Frequency Sleeve Dipole Antenna Tuning

shown in figure 30 was fabricated to hold heavier and more bulky horn antennas for facility measurements not related to this project.

The HP8510 is a coherent, ratio measurement, though absolute power measurements are a capability of the system. The simulated plots were corrected for power levels; however, the actual measurements were adjusted in scale to the power level of the simulation so that the measurements can be overlaid for comparison.

The next section is a comparison of the predicted and measured results. An exception will be noted concerning two antennas in the chamber that were present during the measurement.

6. DATA Comparisons

An exception to the simulation model was made to account for two large antennas that were present in the chamber that could not be removed for the measurements. The antennas were Flam and Russell 6418, diagonal horn antennas with apertures of 2.5 ft. side dimensions. The location of the first horn was at a radius from the center of the turntable of 134.5 ft. at $\phi = 123.88^\circ$. The location of the second horn was at a radius of 138.7 ft. and $\phi = -124.34^\circ$. An approximation of the scattering of the antennas found in references [38] and [39] was added to the simulation model with an antenna cross section approximation given in equation (81).

$$\sigma = Gain \cdot Area = \frac{4\pi A^2}{\lambda^2} \quad (81)$$

A bistatic radar range equation was used to model the antennas where the distance from the antennas to the receive probe antenna changed as the scan occurred.

An overlay of the low frequency, 300 MHz, simulated and measured data is shown in figure 34. The

direct path was also plotted to show the effect of free-space attenuation on the measurement. The standing wave for this chamber configuration was approximately 6 to 10 dB.

A second low frequency simulation was conducted at 300 MHz without the chamber antennas as shown in figure 35. The floor reflection was the most significant scatterer of 2.8 dB. The ceiling was expected to contribute 1.1 dB. The other walls contribute much less in magnitude but at a higher spatial frequency since the path length difference between the direct and secondary path was much greater for the other walls. The path length difference for the floor was approximately one wavelength. The change in the path length difference for the entire floor scan was only approximately 3 inches. Because of these effects and the floor being the most significant contributor, the simulated data always stays positive for the entire scan.

The high frequency, 10 GHz, prediction and scan are shown overlaid in figure 36, and separately in figures 37 and 38, respectfully. The simulated data was limited to a 21 x 21 patch of RAM tips due to the limitations of the VAX disk pack. The ripple levels were between 1 and 2 dB peak-to-peak in the predicted data.

The modal expansion data was expanded to several radii at the locations where scattering sources in the chamber are known to be. The number of data points used was 512. These included the corners of the chamber, the chamber antennas at the opposite ends of the chamber, and the turntable edges. Figure 39 shows the only plot that revealed any significant information in the -90° to -180° sector. This scattering source was probably the chamber antennas mentioned previously and included in the low frequency simulation.

A. Data Correlation The levels of the ripple agrees well between the simulation and the measurements when the chamber antennas were included in the simulation for approximately 90

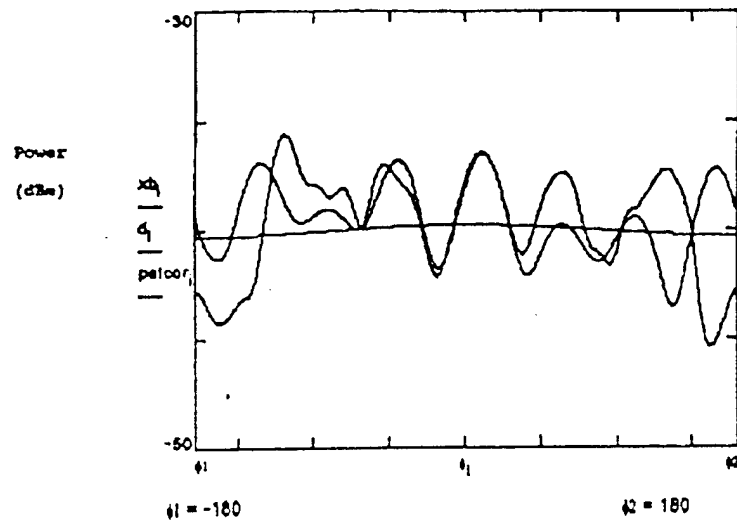


Figure 34 Low Frequency Comparison of Simulated and Measured Data

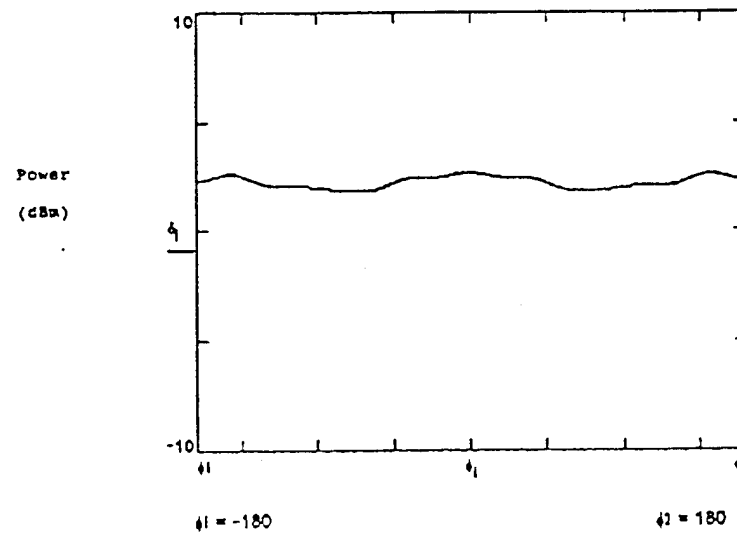


Figure 35 Low Frequency Simulation Without Chamber Antennas

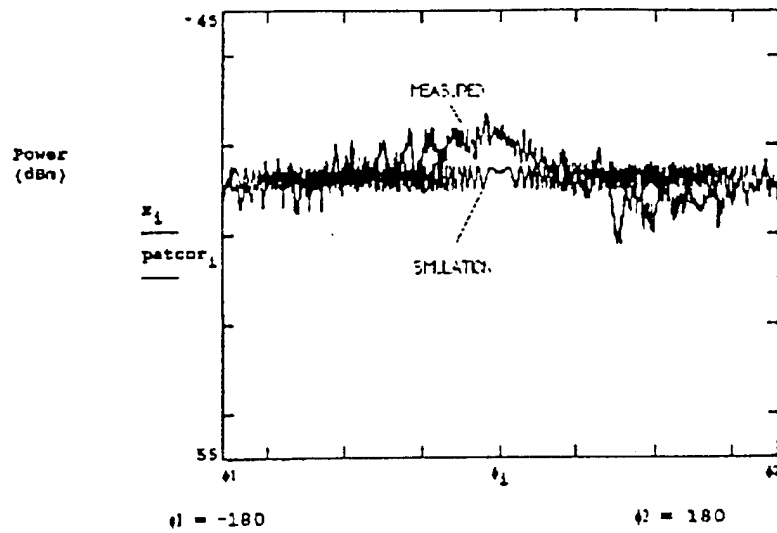


Figure 36 High Frequency Comparison of Simulated and Measured Data

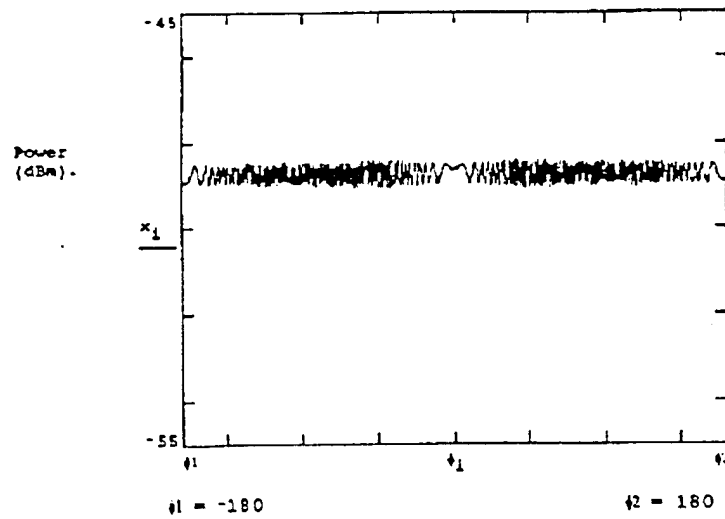


Figure 37 High Frequency Simulation

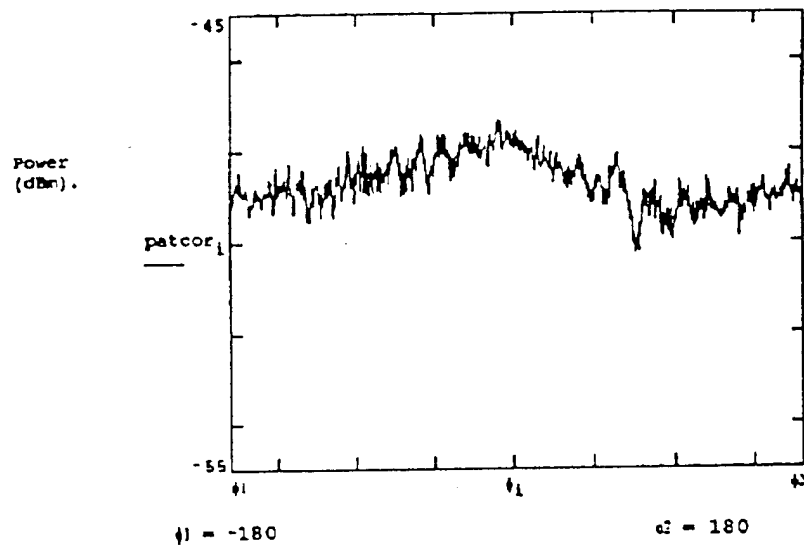


Figure 38 High Frequency Measurement

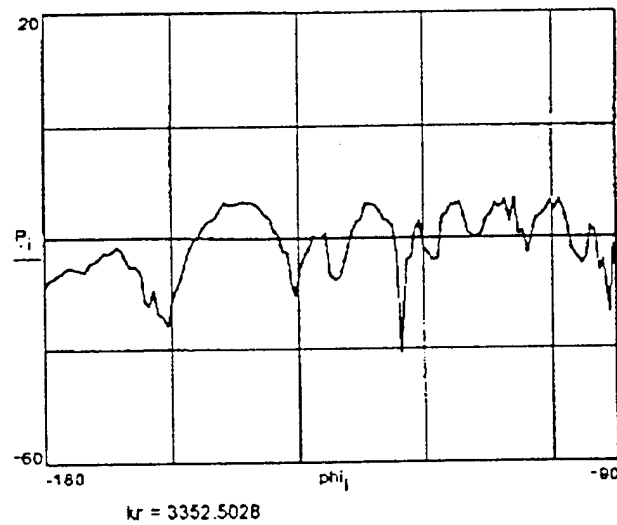


Figure 39 Modal Expansion Showing Phase Convergence in -90° to -180° Sector

% of the scan. However, measurements without the antennas were not possible in the chamber to verify the simulation without these antennas.

The high frequency measurements show approximately a 1 dB higher peak-to-peak ripple than the simulation in 80% of the scan. In the $\pm 40^\circ$ to 70° sector a slightly larger standing wave of approximately 4 dB.

B. Resolving Discrepancies The discrepancies in the high frequency measurements were possibly caused by the manufacturing process of the twisted pyramidal RAM on the floor. It was determined that it was difficult to use the modal expansion diagnostic method in the direction of the source antenna. It was not possible during the measurements to replace the twisted pyramid RAM with other types of RAM to determine the source of the low frequency ripple. The modal expansion was attempted to resolve discrepancies in the high frequency model, although none were found. The resolution of the modal expansion was possibly affected by the 1 GHz frequency sampling interval.

7. CONCLUSIONS

This project was an attempt to improve the quality of chamber characterizations in an anechoic chamber. Computer simulated data was compared to measured data. Good agreement was found between the simulation and measurement for the low frequency data when the Flam and Russell 6418 antennas were included in the simulation. There was good agreement in the high frequency data, except for a slight variation from a low frequency standing wave.

A. Recommendations The following recommendations are made that need to be investigated to improve the simulation and measured data:

1. The physical characteristics of the chamber such as the chamber corners, chamber antennas, input cables, the chamber turntable edges, and the wall behind the range antennas can be included in the modeling.
2. Better constituent parameters need to be obtained for the RAM and concrete materials used in the simulations.
3. A much finer sampling interval was needed for the modal expansion resolution.
4. The low frequency files need to be combined into one program.
5. Linking of more than one disk pack on the VAX computer would allow a larger patch of RAM in the high frequency simulation.
6. The modal expansion scan data would be much more informative in a waterfall plot format.
7. The Flam and Russell 6418 antennas need to be removed from the chamber when they are not being used.

B. Summary A simulation of an anechoic chamber with a cylindrical scan was developed. Ray tracing was used to model the wall scattering with a RAM model used to predict the wall scattering. The simulation was broken up into a low and high frequency model due to the frequency dependant nature of the RAM scattering. The low frequency simulation was developed using a single, specular ray for each wall and the RAM was modeled using a layered, tapered, transmission line method with an anisotropic, inhomogeneous tensor RAM model. The high frequency model was developed using multiple rays on each wall to the tips of the RAM. The tips of the RAM were modeled using TIPBIST.FOR, a bistatic scattering code for a single tip using a dielectric, corner UTD formulation. Each tip is a combination of four edges. Each model sums all of the vectors at the receive probe antenna. A simulation model was included for the range and receive antennas.

Measurements were made in an anechoic chamber and a validation of the simulated data was conducted. The measured data correlated well with the simulation.

A cylindrical scan, modal expansion was developed to resolve discrepancies between the simulated and measured data. The measurements were conducted for incoming waves only using more directional antennas than the characterization probes.

REFERENCES

- [1] King, H. and J. Wong, "Characteristics of a Tapered Anechoic Chamber", *IEEE Trans. Antennas Propagat.*, Vol. AP-15, 1967, p. 488.
- [2] Mansour, M. and J. Jarem, "Anechoic Chamber Design Using Ray Tracing and Theory of Images", *IEEE SOUTHCON 1990 Proc.*, p.689.
- [3] Jarem, J. and M.Mansour, "Finite Difference, Time-Domain Analysis and Ray Tracing Analysis of an Anechoic Chamber", *SCS 1990 Summer Comp. Sim. Conf. Proc.*, p.924.
- [4] Gillette, J., "RF Anechoic Chamber Design Using Ray Tracing", *IEEE AP-S Int. Symp. 1977*, p.250.
- [5] Wu, P., "An Anechoic Chamber Design Technique", *IEEE AP-S Int. Symp. 1977*, p.250.
- [6] Brumley, S., "A Modeling Technique for Predicting Anechoic Chamber RCS Background Levels", *AMTA Annual Symp. Proc. 1987*, p.133.
- [7] Mishra, S. and T.Pavlese, "Design of Absorber-Lined Chambers for EMC Measurements Using a GO Approach", *IEEE Trans. on EMC*, Vol.EMC-26, No.3, Aug., 1984, p.111.
- [8] Mishra, S., "Computer Aided Design of Anechoic Chambers", *AMTA Annual Symp. Proc. 1985*, p.30-1.
- [9] Holloway, C. and E. Kuester, "Modeling Semi-Anechoic Electromagnetic Measurement Chambers", *Univ. of Colo. Dept. of EE Sci. Rept. No. 99*, 1990.
- [10] Arm, M., L.Wolk, M.Rochwarger, R.Reichmeider and N.Erlbvach, "Compact Range Performance Analysis", *AMTA Annual Symp. Proc. 1991*, p.4-19.
- [11] Carey, N., A.Jain and S.Brumley, "Evaluation of Compact Range Design Using Diffuse Surface Ray Tracing Model", *AMTA Annual Symp. Proc. 1991*, p. 7-33.
- [12] Joseph, P., R.Mariano, W.Burnside and I.Gupta, "Analysis of Absorber Scattering in Compact Range Measurement Systems", *AMTA Annual Symp. Proc. 1990*, p.3-31.
- [13] Joseph, P., "A UTD Scattering of Pyramidal Absorber for Design of Compact Range Chambers", *Ph.D. Dissertation, OSU*, 1988.
- [14] Mohamed, M. and J. Jarem, "Errors in Finite-Element Formulation for Lossy Waveguides", *IEEE Proc. 1990 SOUTHEASTCON*, p.177.
- [15] Liepa, V. and C. Cheon, "Analysis and Design of 4-Wire Antenna for Anechoic Chamber Excitation", *IEEE APS Int. Symp. 1989*, p.336.
- [16] Jarem, J., "Electromagnetic Field Analysis of a Four-Wire Anechoic Chamber", *IEEE Trans. Antennas Propagat.*, Vol. AP-38, No.11, Nov.1990, p.1835.
- [17] Devoir, C./Lehman Chambers, Technical Narrative, 1993.

- [18] Bornkessel, C. and H. Uhlmann, "Equivalent Layer Modeling of Pyramidal Absorbers for Field Computations in Anechoic Chambers", *AMTA Annual Symp. Proc.* 1992, p.16-15.
- [19] Jarem, J., "TEM Wave Propagation in a Parallel, Four Wire Anechoic Chamber Enclosure", *IEEE Comp. Soc. 1989 Proc. 21st SE Symp. on Sys. Theory*, p.476.
- [20] Swanstrom, J., "A compact Test Range for Demonstrating Antenna and RCS Measurement Performance", *AMTA Annual Symp. Proc.* 1990, p.12-9.
- [21] Fitzgerald, R., "Using Free-Space Transmission Loss for Evaluating Anechoic Chamber Performance", *IEEE Trans. on EMC*, Vol. EMC-24, No.3, Aug. 1982, p.356.
- [22] Illgen, J. and J. Atkinson, "Anechoic Chamber Modeling", Illgen Simulation Technologies, Inc., Technical Narrative, March 16, 1993, Benefield Anechoic Chamber, Edwards AFB, CA.
- [23] Kuester, E., "The Fundamental Properties of Transversely Periodic Lossy Waveguides", *Univ. of Colo. EE Dept. Sci. Rep. No. 86*, 1986.
- [24] Kuester, E., "Low-Frequency Properties of Transversely Periodic Lossy Waveguides", *Univ. of Colo. EE Dept. Sci. Rep. No. 92*, 1987.
- [25] Kuester, E. and C. Holloway, "Plane-Wave Reflection from Inhomogeneous Uniaxially Anisotropic Absorbing Dielectric Layers", *Univ. of Colo. EE Dept. Sci. Rep. No. 97*, 1989.
- [26] Seville, E., G. Cook, J. Bennett, and E. England, "Location of Environmental Scatterers on a Microwave Antenna Test Range", *AMTA Annual Symp. Proc.* 1992, p.13-3.
- [27] Stratton, J., *Electromagnetic Theory*, McGraw Hill Publ. Comp., 1941.
- [28] Stutzman, W. and G. Thiele, *Antenna Theory and Design*, New York: John Wiley and Sons, Inc., 1981.
- [29] Skolnik, M., *Introduction to Radar Systems*, McGraw Hill Book Comp., 1962, Ch.2.
- [30] ECITF Site Activation Support Task Directive #S910700, Contract Number F04611-89-C-0019, US AFFTC, Doc. # A0011-005-12.
- [31] Anton, H., *Calculus*, Second Ed., John Wiley & Sons, 1984.
- [32] Collin, R., *Foundations for Microwave Engineering*, McGraw-Hill, Inc., 1966.
- [33] *Reference Data for Radio Engineers*, Howard W. Sams & Co., Inc., 1968, 1975.
- [34] *MATHCAD*®, Copyright 1991, MathSoft, Inc.
- [35] Bucci, O., and C. Gennarelli, "Use of Sampling Expansions in Near-Field-Far-Field Transformations: The Cylindrical Case", *IEEE Transac. Antennas Propagat.*, Vol. AP-36, No.6, June, 1988, p. 830.
- [36] *SuperCALC*® Ver. 5.0, Computer Associate, 1989.

[37] Love, A., "The Diagonal Horn Antenna", *Microwave Journal*, March, 1962, p. 117-122.

[38] Hansen, R., "Relationship Between Antennas as Scatterers and as Radiators", *Proceedings of the IEEE*, Vol. 77, No. 5, May, 1989, p. 659.

[39] Lindsey III, J., "Radar Cross-Section Effects Relating to a Horn Antenna", *IEEE Transac. Antennas Propagat.*, Vol. AP-37, No.2, Feb., 1989, p. 257.